Engineering Structures 279 (2023) 115654

Contents lists available at ScienceDirect

Engineering Structures

journal homepage: www.elsevier.com/locate/engstruct

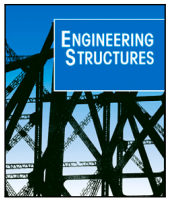

Stress-based form-finding of gridshells for Wire-and-Arc Additive Manufacturing considering overhang constraints

Matteo Bruggi [a,*], Vittoria Laghi [b,c], Tomaso Trombetti [b]

[a] Department of Civil and Environmental Engineering, Politecnico di Milano, 20133, Milano, Italy
[b] Department of Civil, Chemical, Environmental and Materials Engineering, University of Bologna, 40136, Bologna, Italy
[c] Department of Civil and Environmental Engineering, Massachusetts Institute of Technology, 02139, Cambridge, USA

ARTICLE INFO

Keywords:
Form-finding
Wire-and-Arc Additive Manufacturing
Structural optimization
Manufacturing constraints
Local buckling
Overhang constraints

ABSTRACT

The design of spatial truss networks for fabrication using Wire-and-Arc Additive Manufacturing (WAAM) is addressed, combining funicular analysis and optimization. At first, a characterization of the structural behavior of the printed bars is provided based on available experimental tests. Interpolation laws are given both for the yielding stress and the critical stress in compression, depending on the printing direction. Then, dealing with networks with fixed plan projection, a minimization problem is formulated in terms of any independent subset of the force densities and of the height of the restrained nodes. The maximum value of the ratio of the axial force in each branch of the network to the relevant yielding/critical force is adopted as objective function. Local enforcements are prescribed to set lower and upper bounds for the vertical coordinates of the nodes and to control the overhang angle with respect to the vertical direction in the AM process. Gridshells retrieved by the proposed approach are presented and compared to those found when seeking for spatial networks with minimum horizontal reactions, disregarding or considering overhang constraints. Peculiar features of the achieved layouts are pointed out.

1. Introduction

The integration of new digital technologies in construction could lead to more efficient structures. One example is provided by the use of Additive Manufacturing (AM) techniques, which have proved to support the Circular Economy, see e.g. [1], and increase work safety, see e.g. [2,3]. Among various metal AM techniques, Wire-and-Arc Additive Manufacturing (WAAM) results the most suitable to realize large-scale structural components [4–7]. By making use of standard welding equipment mounted on top of robotic arms, elements up to few meters span can be manufactured. Recent research also proved that a severe reduction in CO_2 emission could be reached with WAAM technology, see e.g. [8]. Two alternative printing processes are used in WAAM: (i) the so-called "continuous" printing, which consists in a traditional layer-by-layer deposition and is suitable for planar and shell-like geometries; (ii) the so-called "dot-by-dot" printing, consisting in a spot-like deposition of the welded material to build metal bars for gridshells (double-curvature elements constructed from a grid) and lattice components. Although the application of WAAM in civil engineering was firstly investigated concerning the continuous technique, see e.g. [9–13], a lot of attention is being directed to the potential offered by the dot-by-dot strategy, see e.g. [14–17]. The environmental impact of the construction industry can be further reduced by coupling the AM process with breakthrough design tools for modern architecture, see in particular the methods of computational design [18–20]. The use in recent decades of computational design technologies resulted in the development of new structures with formal freedom and high complexity. However, the current building production still does not allow for such a freedom. Hence, accounting for manufacturing constraints is of paramount importance when aiming at structural efficiency. Lots of effort are being made to leverage the full potential of the combined use of AM and optimization techniques [21]. This is the case of topology optimization [22], which can be tailored to account for peculiar features and limitations related to the adopted manufacturing process, see [23,24]. To give just a few examples, the generation of optimal distributions of material (to maximize a target structural performance) can be coupled to the anisotropic modeling of the printed material, see e.g. [25–27], or endowed with constraints to govern the maximum overhang in layer-by-layer manufacturing to avoid additional supports, see e.g. [28–30].

Form-finding of gridshells is addressed in this work, presenting formulations of optimal design that account for features peculiar to the dot-by-dot WAAM process and to the printed alloy, as derived from

* Corresponding author.
E-mail address: matteo.bruggi@polimi.it (M. Bruggi).

https://doi.org/10.1016/j.engstruct.2023.115654

Available online 18 January 2023

recent experimental investigations. Networks in which loads cause pure axial stresses all over the structural component are considered, aiming at "funicular" shapes. Among the approaches to design spatial truss networks, see e.g. [31–39], a strategy combining the force density method (FDM) [40] and an algorithm of sequential convex programming [21] is implemented for gridshells having fixed projection onto the horizontal plane. Upon introduction of the ratio force to length in each branch of the network, i.e. the element force densities, the equations governing the equilibrium of the nodes may be linearized in terms of their coordinates. For networks with fixed plan projection, i.e. gridshells in which the horizontal coordinates of each node are given and fixed, the equilibrium in the horizontal directions is such that a dependent set of force densities may be identified. This was firstly exploited in the assessment of masonry vaults, using approaches of limit analysis. Independent set of force densities were used in [41] as main unknowns of a best-fit problem. The aim was generating anti-funicular networks matching the mid surface of the arcuated structure to be analyzed, see also [42]. Independent force densities were also used in conjunction with evolutionary algorithms and a hessian-based minimizer in [43], dealing with the design of networks for prescribed horizontal projection and coplanar fixed boundary vertices, see also [44]. In [45], an optimization problem was formulated, using as minimization unknowns not only any set of independent force densities, but also the vertical coordinates of the restrained nodes. Spatial networks of minimum thrust, i.e. minimum horizontal reactions, were sought accounting for local enforcements on the height of the nodes. The analytical form of the problem is such that sequential convex programming, which was originally conceived for problems of size optimization of elastic trusses, may be used to solve efficiently the arising multi-constrained problem. The algorithm is herein extended, testing an alternative objective function and accounting for an additional set of constraints, both actions inspired by some recent experimental results on WAAM-printed bars [46,47].

An experimental investigation was carried out in [47] to characterize the structural behavior of bars produced through dot-by-dot WAAM, under tensile loading. A decay of the elastic modulus and, generally, of the yielding strength was observed for increasing value of the build angle. This is a measure of the orientation of the axis of the printed bar with respect to the vertical direction. Lack-of-straightness was evaluated for two sets of bars, at 0° and 45°, at the ends of the investigated range of build angles. Collapse in compression for dot-by-dot WAAM bars printed along the vertical direction was investigated in [46], for slenderness in the range 30–150.

This contribution aims at introducing formulations of structural optimization that are conceived for the design of gridshells to be fabricated using WAAM. Manufacturing constraints are included in the design process to generate spatial networks that fulfill overhang limitations. The stress regime is evaluated/controlled in each one of the branches by defining capacity laws, both in tension and in compression, which are derived from the analysis of the available experimental data on WAAM-printed bars.

More in detail, the formulation used in [45] is endowed with overhang constraints to enforce a maximum build angle equal to 45°. The interval 0°–45° is that investigated in the referenced experimental tests, as commonly used in practice when employing dot-by-dot WAAM. Two objective functions are considered. As an alternative to the design for minimum thrust, a stress-based design is investigated by minimizing the maximum ratio of the value of the axial force acting in each element to the relevant yielding and critical forces, both depending on the build angle of the bar. To this goal, a smooth approximation is employed to interpolate experimental yielding forces, whereas the use of the Perry–Robertson capacity formula [48] is assessed for vertically printed bars, and then extended to the case of varying build angle. Numerical simulations show that the considered multi-constrained problem can be effectively solved through the Methods of Moving Asymptotes (MMA) [49]. Gridshells retrieved by the proposed stress-based approach are presented and compared to those found when seeking for spatial networks with minimum horizontal reaction, with or without overhang constraints. Peculiar features of the achieved optimal solutions are discussed.

In the remainder of this paper, Section 2 is concerned with the material characterization of the bars printed by dot-by-dot WAAM, Section 3 recalls fundamentals of the linear force density method, focusing on networks with prescribed horizontal projection, Section 4 introduces the considered optimization problems, Section 5 reports the numerical simulations, with focus on mechanical and manufacturing issues. Section 6 concludes the paper, summarizing the main results of this work.

2. Dot-by-dot WAAM: material characterization

2.1. Elastic modulus, yielding stress, and lack-of-straightness

An extended experimental investigation was performed in [47] on dot-by-dot wire-and-arc additively manufactured 304L stainless steel bars, pointing out that the printing direction affects the yielding stress and the Young's modulus of the built alloy. In general, both diminish when diverging from the vertical deposition of material. Three sets of bars were tested in tension, considering the cases $\alpha = 0°$, 10°, and 45°, being α the build angle, i.e. the orientation of the printing direction with respect to the vertical axis, see Fig. 1(a). Larger overhangs are not common in dot-by-dot WAAM, due to issues affecting the printing process and reliability of the printed component.

The mechanical response in tension was evaluated in terms of key effective mechanical parameters from the volume-equivalent uniform cylinder, for a total of 29 specimens. The diameter d of the (nearly)-circular effective cross-section of the bars was found equal to 6 mm.

Based on the available data, the following interpolation laws are proposed for the elastic modulus E and the yielding stress σ_Y, respectively, in the range $0° \le \alpha \le 45°$:

$$E(\alpha) = 98 + 35\exp(-8\tan\alpha), \quad \text{(GPa)}, \tag{1a}$$

$$\sigma_Y(\alpha) = 208 + 35\exp(-8\tan\alpha), \quad \text{(MPa)}, \tag{1b}$$

see Fig. 2. Eq. (1a) fits well the observed decrease in terms of average values of the elastic modulus. To be on the safe side, the same decay rate is adopted for σ_Y in Eq. (1b).

During the experimental investigation, the lack-of-straightness of the printed specimens was measured for the cases $\alpha = 0°$ and $\alpha = 45°$. The eccentricity between the real axis, locus of centroids of the printed cross-sections, and an ideal straight axis, see Fig. 1(d), was evaluated for a few specimens. An average value over the length of the bar was computed for each one of the two cases. This value was found equal to $0.0022l$ and $0.0028l$, for $\alpha = 0°$ and $\alpha = 45°$ respectively, being l the length of the bar. The following interpolation is used to deal with the eccentricity of the axis of the bar e depending on the printing inclination $0° \le \alpha \le 45°$:

$$e(\alpha) = \big(0.00315 - 0.00095\exp(-\tan\alpha)\big)l. \tag{2}$$

2.2. Critical stress in compression

Accounting for Eqs. (1) and (2) in the Perry–Robertson capacity formula [48], the collapse behavior of WAAM bars in compression can be predicted in a significant range of slenderness. The rationale of this criterion is that a strut undergoes an initial deflection represented by the eccentricity parameter e, whereas collapse occurs when the ultimate stress σ_Y is reached in the most loaded cross-section. Accordingly,

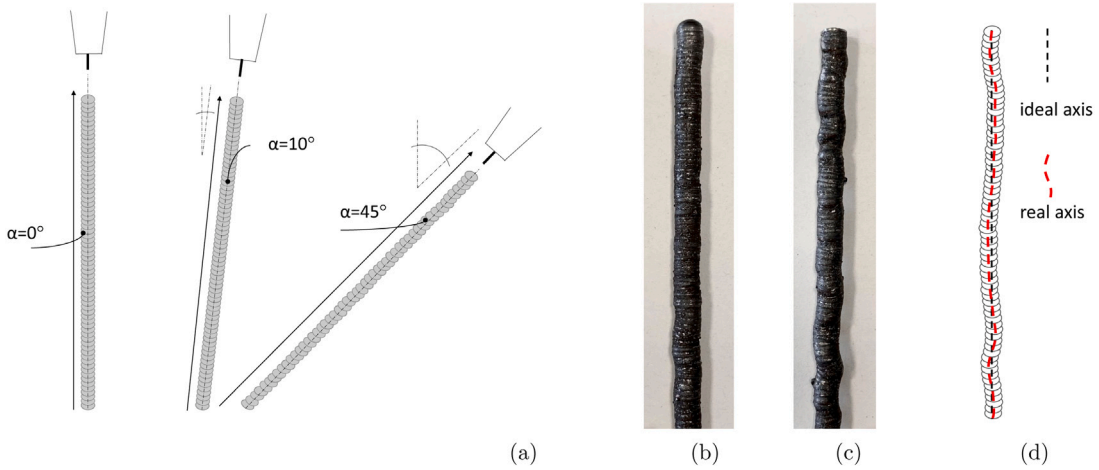

Fig. 1. Dot-by-dot WAAM specimens tested in [47]: orientation of the axis of the printed bars with respect to the vertical direction during the AM process, schematic adapted from [47] (a); close-up of a bar printed with $\alpha = 0°$ (b); close-up of a bar printed with $\alpha = 45°$ (c); schematic of the lack-of-straightness (d).

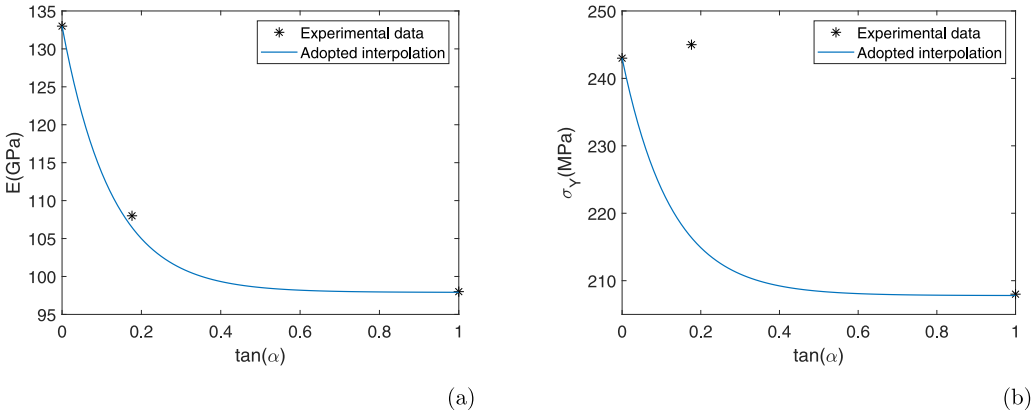

Fig. 2. Material laws for WAAM bars in the range $\alpha = 0°$–$45°$ vs. experimental results: $E - \tan\alpha$ (a); $\sigma_Y - \tan\alpha$ (b).

denoting by l_e the effective length of the strut, the slenderness λ and the relative slenderness λ_r of the bar are defined as:

$$\lambda = \frac{l_e}{r_z}, \quad \lambda_r(\alpha) = \frac{\lambda}{\pi}\sqrt{\frac{\sigma_Y(\alpha)}{E(\alpha)}}, \tag{3}$$

where r_z is the radius of gyration of the cross-section, which equals $d/4$ for the herein considered circular section. Denoting by P the compressive force exerted on the strut, by A the area of the cross-section (herein $\pi/4d^2$) and by k_z its kernel radius (herein $d/8$), the critical stress $\sigma_c(\alpha) = P/A$ that causes failure in compression may be recovered by solving the following quadratic equation, see [50]:

$$\lambda_r^2(\alpha)\left(\frac{\sigma_c(\alpha)}{\sigma_Y(\alpha)}\right)^2 - \left(\lambda_r^2(\alpha) + 1 + \frac{e(\alpha)}{k_z}\right)\frac{\sigma_c(\alpha)}{\sigma_Y(\alpha)} + 1 = 0. \tag{4}$$

The solution may be written explicitly as:

$$\frac{\sigma_c(\alpha)}{\sigma_Y(\alpha)} = c_\alpha - \sqrt{c_\alpha^2 - \frac{1}{\lambda_r^2(\alpha)}}, \quad \text{where} \quad c_\alpha = \frac{1}{2\lambda_r^2(\alpha)}\left(\lambda_r^2(\alpha) + 1 + \frac{e(\alpha)}{k_z}\right). \tag{5}$$

As reported in [46], compression tests were performed on dot-by-dot wire-and-arc additively manufactured 304L stainless steel bars for $\alpha = 0°$ only, with different lengths. The aim of these tests was evaluating the mechanical response of the bars for different slenderness values, from stub to very slender specimens. Compression tests were performed in displacement control with an initial velocity of 0.2 mm/min, operating an unloading after 6-mm displacement at 0.4 mm/min, and reloading at 0.2 mm/min until 12-mm displacement. The bars were restrained in order to obtain a hinge-clamped configuration, that means $l_e = 0.9l$.

For $\alpha = 0°$, the critical stress σ_c predicted by Eq. (5) is represented in Fig. 3(a) as a function of the slenderness λ. The aforementioned experimental data are reported in the same graph, for comparison. A very good agreement of the capacity formula and the experimental results is found, with the only exception of a short bar for which the implemented criterion underestimates the capacity (thus remaining on the safe side).

In Fig. 3(b) a few curves $\sigma_c(\alpha)$, $F_c(\alpha)$ vs. λ are sketched to highlight the effect of the printing orientation on the critical stress over a significant range of slenderness values ($0° \le \alpha \le 45°$).

The same type of bars will be addressed in Section 5, with the assumption $l_e = l$.

3. Force density method for networks with fixed plan projection

A cartesian reference system with axes x, y, and z is considered. The force density method is used to handle the equations governing the equilibrium of truss spatial networks. Following the original notation used in [40], the net is made of m elements connecting n_s nodes.

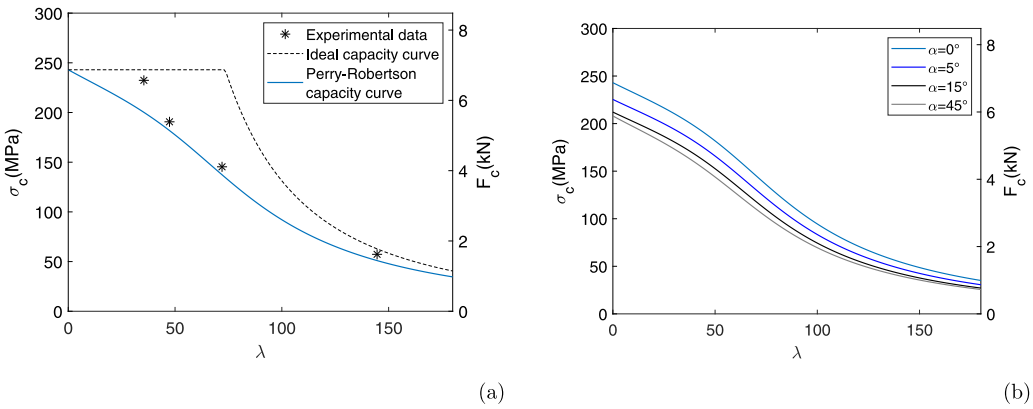

Fig. 3. Capacity formula for WAAM bars: Perry–Robertson and ideal $\sigma_c(F_c)$-λ curves for $\alpha = 0°$ vs. experimental results (a); Perry–Robertson $\sigma_c(F_c)$-λ curves in the range $\alpha = 0°$–$45°$ (b).

When external loads are applied at the n unrestrained nodes, branches undergo axial forces only, while reactions arise at the n_f restrained ones ($n_s = n + n_f$). The vectors $\mathbf{u}$, $\mathbf{v}$, $\mathbf{w}$ store the coordinate difference of the connected points along the axis x, y, z, respectively, i.e.:

$$\mathbf{u} = \mathbf{C}_s\mathbf{x}_s = \mathbf{C}\mathbf{x}+\mathbf{C}_f\mathbf{x}_f, \quad \mathbf{v} = \mathbf{C}_s\mathbf{y}_s = \mathbf{C}\mathbf{y}+\mathbf{C}_f\mathbf{y}_f, \quad \mathbf{w} = \mathbf{C}_s\mathbf{z}_s = \mathbf{C}\mathbf{z}+\mathbf{C}_f\mathbf{z}_f, \tag{6}$$

where $\mathbf{C}_s$ is the connectivity matrix depending on the topology of the grid, and $\mathbf{x}_s$, $\mathbf{y}_s$, $\mathbf{z}_s$ are vectors that gather the coordinates of the nodes. Subsets $\mathbf{C}$ and $\mathbf{C}_f$ refer to the unrestrained and restrained nodes, whose coordinates are respectively stored in $\mathbf{x}$, $\mathbf{y}$, $\mathbf{z}$, and $\mathbf{x}_f$, $\mathbf{y}_f$, $\mathbf{z}_f$. Introducing $\mathbf{U} = \mathrm{diag}(\mathbf{u})$, $\mathbf{V} = \mathrm{diag}(\mathbf{v})$ and $\mathbf{W} = \mathrm{diag}(\mathbf{w})$, the equilibrium equations read:

$$\begin{bmatrix} \mathbf{C}^T\mathbf{U}\mathbf{L}^{-1} \\ \mathbf{C}^T\mathbf{V}\mathbf{L}^{-1} \\ \mathbf{C}^T\mathbf{W}\mathbf{L}^{-1} \end{bmatrix}\mathbf{s} = \begin{bmatrix} \mathbf{p}_x \\ \mathbf{p}_y \\ \mathbf{p}_z \end{bmatrix}, \tag{7}$$

where $\mathbf{s}$ gathers the forces in the m branches and $\mathbf{p}_x$, $\mathbf{p}_y$, $\mathbf{p}_z$ are the components along the cartesian axes of the point loads at the unrestrained nodes. $\mathbf{L} = \mathrm{diag}(\mathbf{l})$ is a square matrix that collects, along its diagonal, the length of the branches of the net, being $l_i = \sqrt{u_i^2 + v_i^2 + w_i^2}$. The definition of the force densities vector $\mathbf{q} = \mathbf{L}^{-1}\mathbf{s}$ allows re-writing the equilibrium of the unrestrained nodes of the spatial network as:

$$\begin{bmatrix} \mathbf{C}^T\mathbf{U} \\ \mathbf{C}^T\mathbf{V} \\ \mathbf{C}^T\mathbf{W} \end{bmatrix}\mathbf{q} = \begin{bmatrix} \mathbf{p}_x \\ \mathbf{p}_y \\ \mathbf{p}_z \end{bmatrix}, \tag{8}$$

i.e. a system of linear equations that are uncoupled in the three cartesian directions.

In case of networks with fixed plan projection, see in particular [41–44,51], the horizontal equilibrium of the unrestrained nodes may be gathered in the following system of equations:

$$\begin{bmatrix} \mathbf{C}^T\mathrm{diag}(\mathbf{C}_s\mathbf{x}_{s0}) \\ \mathbf{C}^T\mathrm{diag}(\mathbf{C}_s\mathbf{y}_{s0}) \end{bmatrix}\mathbf{q} = \begin{bmatrix} \mathbf{p}_x \\ \mathbf{p}_y \end{bmatrix}, \tag{9}$$

where the vector $\mathbf{x}_{s0}$ and $\mathbf{y}_{s0}$ store the prescribed and fixed x and y coordinate of the nodes, respectively. If the rank of the coefficient matrix is equal to that of the augmented matrix, the network is suitable to withstand $\mathbf{p}_x$ and $\mathbf{p}_y$. By applying Gauss–Jordan elimination [52] to Eq. (9), a set of $m - r$ independent force densities $\overline{\mathbf{q}}$ can be detected, being r the rank. The r dependent force densities in $\widetilde{\mathbf{q}}$ may be re-written in terms of the independent ones as:

$$\widetilde{\mathbf{q}} = \mathbf{B}\overline{\mathbf{q}} + \mathbf{d}, \tag{10}$$

where $\mathbf{B}$ and $\mathbf{d}$ are matrices whose constant entries only depend on the topology of the network and on the prescribed horizontal load, if any. Upon introduction of $\mathbf{Q} = \mathrm{diag}(\mathbf{q})$, the vertical coordinates of the unrestrained nodes can be computed by solving the equilibrium along the z axis, i.e.:

$$\mathbf{C}^T\mathbf{Q}\mathbf{C}\mathbf{z} + \mathbf{C}^T\mathbf{Q}\mathbf{C}_f\mathbf{z}_f = \mathbf{p}_z. \tag{11}$$

As observed e.g. in [53], it is not straightforward to control the coordinates of the nodes using the force density method. In the following section, an optimization approach is formulated that enforces limitations on the height of the nodes, and on the related orientation of the connecting branches, through local constraints.

4. Form-finding of spatial networks for WAAM

Based on the outcome of Sections 2 and 3, a problem of optimal design of WAAM spatial networks with fixed plan projection is formulated. A multi-constrained minimization is stated in terms of any reduced set of independent force densities $\overline{\mathbf{q}}$ and of the vertical coordinates of the restrained nodes $\mathbf{z}_f$. It reads:

$$\begin{cases} \min\limits_{\overline{\mathbf{q}},\ \mathbf{z}_f} & f & \text{(a)} \\ \text{s.t.} & \widetilde{\mathbf{q}} = \mathbf{B}\overline{\mathbf{q}} + \mathbf{d}, & \text{(b)} \\ & \mathbf{C}^T\mathbf{Q}\mathbf{C}\mathbf{z} + \mathbf{C}^T\mathbf{Q}\mathbf{C}_f\mathbf{z}_f = \mathbf{p}_z, & \text{(c)} \\ & \left(\frac{\tan\alpha_i}{\tan\alpha_{max}}\right)^2 \le 1 \quad \text{for } i = 1,\dots,m, & \text{(d)} \\ & z_j(\overline{\mathbf{q}},\mathbf{z}_f) \ge z_j^{min} \quad \text{for } j = 1,\dots,n, & \text{(e)} \\ & z_j(\overline{\mathbf{q}},\mathbf{z}_f) \le z_j^{max} \quad \text{for } j = 1,\dots,n, & \text{(f)} \\ & z_{fh}^{min} \le z_{fh} \le z_{fh}^{max} \quad \text{for } h = 1,\dots,n_f, & \text{(g)} \end{cases} \tag{12}$$

where $\tan\alpha_i$, which is the tangent of the angle between the vertical direction and the printing direction for the ith bar, may be computed as:

$$\tan\alpha_{ix} = \left(\frac{v_i^2 + w_i^2}{u_i^2}\right)^{\frac{1}{2}}, \quad \text{or} \quad \tan\alpha_{iy} = \left(\frac{u_i^2 + w_i^2}{v_i^2}\right)^{\frac{1}{2}}, \quad \text{or} \quad \tan\alpha_{iz} = \left(\frac{u_i^2 + v_i^2}{w_i^2}\right)^{\frac{1}{2}}, \tag{13}$$

if the vertical direction, during AM, is aligned with the x, y, or z axis, respectively; α_{max} is the maximum allowed value of the build angle, i.e. the maximum admissible overhang.

In the above formulation, Eq. (12b) allows recovering the dependent force densities $\widetilde{\mathbf{q}}$ from the independent set $\overline{\mathbf{q}}$. Eq. (12c) is the equilibrium of the unrestrained nodes in the vertical direction, to compute $\mathbf{z}$ from the minimization unknowns $\overline{\mathbf{q}}$ and $\mathbf{z}_f$. General loading conditions can be addressed through the proposed formulation, see also [45]. Under the assumption of networks with fixed plan projection, the horizontal components of the nodal forces ($\mathbf{p}_x$ and $\mathbf{p}_y$) affect the

result of the Gauss–Jordan elimination performed on Eq. (9), i.e. the sets of dependent and independent force densities and the relationship that links the former to the latter. Design-dependent loads, such as self-weight, can be straightforwardly accounted for through a continuation approach. The optimization problem in Eq. (12) must be solved repeatedly, updating the load vector at the end of each run.

Eq. (12d) enforces the overhang constraints, prescribing the maximum value of the deviation of the printing direction of each branch of the network from the vertical one. The coordinate difference of the connected points given in Eq. (6) are used to enforce this geometrical constraint. Dealing with grids having fixed plan geometry, $\mathbf{u}$ and $\mathbf{v}$ do not depend on the minimization unknowns, whereas it is recalled that $\mathbf{w}(\overline{\mathbf{q}}, \mathbf{z}_f)$. According to Section 2, the assumption $\alpha_{max} = 45°$ is used in the numerical studies that follow.

Eqs. (12e)–(12f) are two sets of inequalities that prescribe lower and upper limits for $\mathbf{z}$. The design domain is such that each one of the n coordinates z_j should be bounded from below by z_j^{min} and from above by z_j^{max}. Finally, Eq. (12g) deals with side constraints for the minimization unknowns z_{fh}, enforcing lower and upper limits for the restrained nodes.

Different objective functions can be considered in the formulation of Eq. (12). The horizontal reactions of the network can be minimized by adopting:

$$f = f_r = \sum_h^{n_f} \left(R_{xh}^2 + R_{yh}^2 \right), \tag{14}$$

where the vector storing the components of the reactions along the x and y direction, $\mathbf{R}_x$ and $\mathbf{R}_y$ respectively, can be computed as $\mathbf{R}_x = \mathbf{C}_f^T \mathrm{diag}(\mathbf{C}_s \mathbf{x}_{s0})\mathbf{q}$ and $\mathbf{R}_y = \mathbf{C}_f^T \mathrm{diag}(\mathbf{C}_s \mathbf{y}_{s0})\mathbf{q}$, see e.g. [45].

Alternatively, a stress-based design of the spatial network may be achieved by implementing:

$$f = f_s = \max \left(\frac{s_i}{s_{Yi}}, -\frac{s_i}{s_{ci}}, \dots, \frac{s_m}{s_{Ym}}, -\frac{s_m}{s_{cm}} \right), \tag{15}$$

where:

- $s_{Yi} = A\,\sigma_Y(\alpha_i)$ is the maximum value of the axial force that the ith of the m branches of the network can undergo prior to yielding, depending on the printing orientation, see Eq. (1b);
- $s_{ci} = A\,\sigma_c(\alpha_i)$ is the critical force in compression which is a function of the printing orientation, see the capacity formula of Eq. (5).

It is remarked that the force vector reads $\mathbf{s} = \mathbf{L}\mathbf{q}$, meaning that f_s depends on both sets of minimization unknowns $\mathbf{q}$ and $\mathbf{z}_f$.

Objective functions from truss design could be implemented as further alternatives. Reference is made in particular to [43,54], minimizing the so-called load-path function in order to find the lightest design for a given stress in all the branches of the truss.

Due to its peculiar form, the multi-constrained optimization problem in Eq. (12) can be efficiently solved through techniques of sequential convex programming that were originally conceived to handle multi-constrained problems of size optimization, see [45]. The Method of Moving Asymptotes (MMA) [49] is a first order method that implements approximations for the objective functions and constraints in the direct or the inverse variable depending on the sign of the gradient. It is extensively used in topology optimization, see e.g. [55]. It must be remarked that the max function in Eq. (15) can make the problem non-smooth (i.e. non-differentiable), which is troublesome for gradient-based optimization. However, this problem is addressed in the present work by using a min–max formulation. MMA may handle both the minimization problem arising for $f = f_r$, and the min–max problem formulated for $f = f_s$. In the latter case, an equivalent formulation is solved by MMA, see [56]. It reads:

$$\begin{cases} \min\limits_{\overline{\mathbf{q}},\ \mathbf{z}_f} & c & \text{(a)} \\ \text{s.t.} & \widetilde{\mathbf{q}} = \mathbf{B}\overline{\mathbf{q}} + \mathbf{d}, & \text{(b)} \\ & \mathbf{C}^T\mathbf{Q}\mathbf{C}\mathbf{z} + \mathbf{C}^T\mathbf{Q}\mathbf{C}_f\mathbf{z}_f = \mathbf{p}_z, & \text{(c)} \\ & c \geq \frac{s_i}{s_{Yi}} \quad \text{for } i = 1, \dots, m, & \text{(d)} \\ & c \geq -\frac{s_i}{s_{ci}} \quad \text{for } i = 1, \dots, m, & \text{(e)} \\ & c \geq 0, & \text{(f)} \\ & \left(\frac{\tan\alpha_i}{\tan\alpha_{max}} \right)^2 \leq 1 \quad \text{for } i = 1, \dots, m, & \text{(g)} \\ & z_j(\overline{\mathbf{q}}, \mathbf{z}_f) \geq z_j^{min} \quad \text{for } j = 1, \dots, n, & \text{(h)} \\ & z_j(\overline{\mathbf{q}}, \mathbf{z}_f) \leq z_j^{max} \quad \text{for } j = 1, \dots, n, & \text{(i)} \\ & z_{fh}^{min} \leq z_{fh} \leq z_{fh}^{max} \quad \text{for } h = 1, \dots, n_f. & \text{(j)} \end{cases} \tag{16}$$

In Section 5, Eqs. (12) and (16) are solved by handling the whole set of local constraints. It must be remarked that the computational cost of such an approach increases rapidly with the size of the application. The augmented Lagrangian method could be conveniently adopted as an efficient alternative, replacing the original multi-constrained optimization problem by a sequence of bound constrained optimization subproblems. This method has proven successful in handling very large scale problems of stress-constrained topology optimization, with a similar form as Eqs. (12) and (16), but, generally, a much larger number of minimization unknowns. Reference is made to discussions and applications in [57,58].

The computation of the gradient of the objective function and of the constraints is required to run MMA. This is a straightforward task, once the sensitivity of $\mathbf{q}$ and $\mathbf{z}$ with respect to both sets of minimization unknowns $\overline{\mathbf{q}}$ and $\mathbf{z}_f$ is available.

The sensitivity of $\widetilde{\mathbf{q}}$ with respect to the kth component of the vector $\overline{\mathbf{q}}$ is found by differentiation of Eq. (10). According to the same equation, the derivative of $\widetilde{\mathbf{q}}$ with respect to any component of $\mathbf{z}_f$ is equal to zero. The sensitivity of $\mathbf{z}$ may be computed looking at Eq. (11). Under the assumption of design-independent loads, the derivative of $\mathbf{z}$ with respect to the kth component of the vector $\overline{\mathbf{q}}$ is:

$$\frac{\partial \mathbf{z}}{\partial \overline{q}_k} = (\mathbf{C}^T\mathbf{Q}\mathbf{C})^{-1} \left[-\mathbf{C}^T \frac{\partial \mathbf{Q}}{\partial \overline{q}_k}\mathbf{C}\mathbf{z} - \mathbf{C}^T \frac{\partial \mathbf{Q}}{\partial \overline{q}_k}\mathbf{C}_f\mathbf{z}_f \right], \tag{17}$$

where $\partial\mathbf{Q}/\partial\overline{q}_k$ is computed remembering that $\mathbf{Q} = \mathrm{diag}(\mathbf{q})$. Similarly, the derivative of $\mathbf{z}$ with respect to the hth component of the vector $\mathbf{z}_f$ is:

$$\frac{\partial \mathbf{z}}{\partial z_{fh}} = (\mathbf{C}^T\mathbf{Q}\mathbf{C})^{-1} \left[-\mathbf{C}^T\mathbf{Q}\mathbf{C}_f \frac{\partial \mathbf{z_f}}{\partial z_{fh}} \right], \tag{18}$$

where $\partial\mathbf{z_f}/\partial z_{fh}$ is the null vector except for a unitary entry at the hth position.

The sensitivity of the objective function f_r calls for $\partial\mathbf{q}/\partial\overline{q}_k$ only, see also [51].

The sensitivity of $\tan\alpha_i$ can be computed by differentiation of Eqs. (13), depending on the selected printing orientation. Due to the assumption of networks with fixed plan projection, only the term w_i is a function of the minimization unknowns. The relevant derivatives may be computed by differentiation of Eq. (6). They read:

$$\frac{\partial \mathbf{w}}{\partial \overline{q}_k} = \mathbf{C}\frac{\partial \mathbf{z}}{\partial \overline{q}_k}, \qquad \frac{\partial \mathbf{w}}{\partial z_{fh}} = \mathbf{C}\frac{\partial \mathbf{z}}{\partial z_{fh}} + \mathbf{C}_f\frac{\partial \mathbf{z_f}}{\partial z_{fh}}. \tag{19}$$

It must be remarked that the derivatives of $\tan\alpha_i$ with respect to the minimization unknowns are required not only to compute the sensitivity of the overhang constraints, but also to evaluate the derivatives of the yielding force, s_{Yi}, and of the critical force in compression, s_{ci}, in f_s. Both quantities depend on $\tan\alpha_i$, see Eqs. (5) and (1b), respectively.

Recalling that $s_i = \sqrt{u_i^2 + v_i^2 + w_i^2}\,q_i$, the sensitivity of the element forces $\mathbf{s}$ with respect to the minimization unknowns $\overline{\mathbf{q}}$ and $\mathbf{z}_f$ can be written in terms of the derivatives of $\mathbf{w}$ and $\mathbf{q}$.

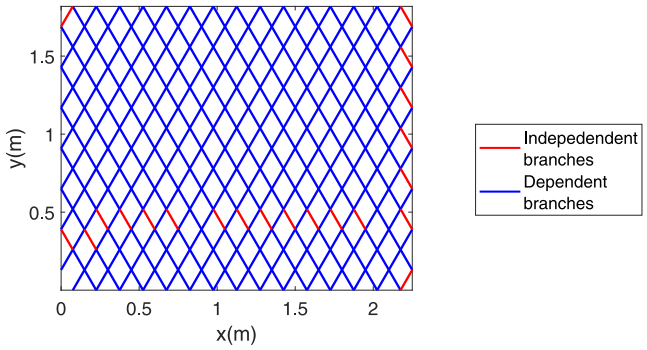

Fig. 4. Example 1. Fixed plan geometry for the generation of optimal spatial networks. Independent branches are marked in red. (For interpretation of the references to color in this figure legend, the reader is referred to the web version of this article.)

5. Numerical simulations

Numerical simulations are presented to assess the proposed approach. Section 5.1 addresses preliminary simulations concerning anti-funicular networks, Section 5.2 deals with funicular ones, while Section 5.3 is concerned with gridshells having a saddle-like shape. Section 5.4 addresses a network with repetitive structure. The problems presented in Section 4 are implemented, providing comparisons among the achieved layouts.

Diamond-like gridshells are considered in the present study. In the (fixed) projection onto the horizontal plane, branches have length $l_{xy} = 0.15\,\text{m}$, if not differently specified, with a reciprocal angle of 60° or 120°. A reference load is addressed, if not differently specified. It consists of nodal forces equal to 1 N acting along the z axis all over the network. This may be also regarded as a rough approximation (by excess) of the weight of the dot-by-dot WAAM network, the latter reading 2.2 N/m.

At first, the minimum thrust design (with $f = f_r$) is investigated, focusing on the sensitivity of the solution to the enforcement of the overhang constraints. Then, stress-based layouts are generated (for $f = f_s$) and compared to those found through the minimization of the horizontal reactions. The same starting guess has been used to initialize all the formulations tested when dealing with the same example. Two starting points have been investigated in Section 5.1 to address convergence features of the proposed approach. In all the pictures representing funicular networks, the symbols + and ∘ stand for points where the nodes of the network touch the extrados and the intrados of the prescribed design region, respectively. Maps of the forces computed in the branches of the network under the reference load are provided.

5.1. Example 1

A rectangular bay with overall size $d_x = 5.50\,\text{m} \times d_y = 3.62\,\text{m}$ is addressed. Exploiting symmetry, only one fourth of the bay is considered in this preliminary investigation. Fig. 4 shows the fixed plan geometry used in the generation of the optimal spatial networks. The nodes lying at $x = 0\,\text{m}$ and those at $y = 0\,\text{m}$ are fully restrained. Restraints along the x axis are enforced at $x = 2.25\,\text{m}$, whereas restraints along the y axis are prescribed at $y = 1.81\,\text{m}$. By applying Gauss–Jordan elimination to the system governing the horizontal equilibrium, see Eq. (9), it is found that $r = 370$ dependent force densities exist, out of $m = 391$ branches. The elements marked in red in the picture are those belonging to the set of $m - r = 21$ independent force densities employed in the simulations. Indeed, the optimization problem of Eq. (12) is set up in terms of 43 parameters (21 force densities and 22 vertical coordinates of the nodes that are restrained along the z axis). The lower bound and the upper bound of the height of the unrestrained nodes read $z^{min} = 2.5\,\text{m}$ and $z^{max} = 3.5\,\text{m}$, respectively. This set of conditions is enforced through $2 \cdot n = 390$ local constraints, see Eqs. (12e)–(12f). Side constraints are such that the same variation in height is allowed to the nodes along the fully restrained edges, i.e. $z_f^{min} = 2.5\,\text{m}$ and $z_f^{max} = 3.5\,\text{m}$ $\forall h$ in Eq. (12g).

Aiming at designing anti-funicular networks, side constraints $\overline{q}_k \leq 0$ are implemented $\forall k$. The starting guess for the minimization algorithm is $\overline{q}_k = -50\,\text{N/m}$ $\forall k$, in conjunction with $z_{fh} = (z_{fh}^{min} + z_{fh}^{max})/2 = 3\,\text{m}$ $\forall h$.

At first, a problem of minimum thrust is investigated, adopting as objective function f_r of Eq. (14), while disregarding the overhang constraints of Eq. (12d). The optimal gridshell, along with a map of the forces acting in the branches, is represented in Fig. 5(a). All the fully restrained nodes have height equal to the prescribed lower bound z_f^{min}, whereas a few nodes in the middle of the bay have the z coordinate equal to z^{max}. This allows maximizing the slope of the members along the perimeter of the bay, thus minimizing the horizontal component of the reactions. Looking at the forces in the branches, the maximum compressive force among all s_i reads $-11.05\,\text{N}$, whereas the maximum value of the ratio $-s_i/s_{ci}$ (force to critical compressive force in each branch) is $9.4 \cdot 10^{-3}$.

In Wire-and-Arc Additive Manufacturing, it is quite frequent to build complex shapes by printing a few parts separately and, then, assembling the components into the final structure. A favorable setting to produce the designed quarter gridshell consists in orienting the part, during the AM process, such that the y axis is aligned to the vertical direction. In this configuration, the overhang angles are much lower than those found when building with the vertical axis aligned to the z (or x) axis. The four parts may be subsequently oriented and assembled to create the final layout of the gridshell, the one in which the vertical direction matches the z axis. In Fig. 5(b), a map of the element values of the squared ratio $(\tan\alpha_{iy}/\tan\alpha_{max})^2$ is given. Notwithstanding the adoption of the y axis as the vertical direction during the manufacturing process, the build angle of most bars exceeds the allowed limit $\tan\alpha_{max} = 1$ by far. The first row in Table 1 provides a summary of the above data, including the value of the objective function f_r at convergence and the total length of the members constituting the spatial networks.

A further optimization run is performed including the set of the overhang constraints, i.e. considering the whole problem in Eq. (12) with $f = f_r$ and local control of the element build angles α_{iy}. This calls for additional $m = 391$ enforcements. The achieved optimal design is depicted in Fig. 6(a), along with a map of the element forces. Values of the squared ratio $(\tan\alpha_{iy}/\tan\alpha_{max})^2$, i.e. of the left hand side of the set of inequality constraints in Eq. (12d), are given in Fig. 6(b) for all the branches of the network. A layout that is fully feasible with respect to the overhang limitations is found, at the cost of an increase in the objective function, see second row in Table 1. In comparison with the optimal solution of Fig. 5(a), most of the nodes along the perimeter have a larger height, such that the network is shallower. This is needed to meet the requirement on the admissible build angle (especially for the outer bars of the network), but is detrimental for the magnitude of the horizontal component of the reactions. A minor increase in terms of maximum compressive force is reported with respect to the previous case. However, the maximum value of the ratio $-s_i/s_{ci}$ is smaller.

A final investigation is performed addressing a stress-based design, which includes accounting for the overhang constraints on the element angles α_{iy}. Indeed, the whole problem in Eq. (12) is considered adopting $f = f_s$, which means minimizing the maximum value of the ratio $-s_i/s_{ci}$ over the anti-funicular network, i.e. solving Eq. (16). The final layout with the map of the element forces is given in Fig. 7(a), whereas feasibility of the build angles may be checked in Fig. 7(b). As expected, the achieved layout exhibits the minimum value of f_s among the presented networks, see third row in Table 1. This comes with the highest value of the maximum compressive force read in the bars. Indeed, in each branch, the critical force in compression primarily depends on the slenderness of the element (herein the length, because of the given cross-section) and, to a lesser extent, on the build angle, see

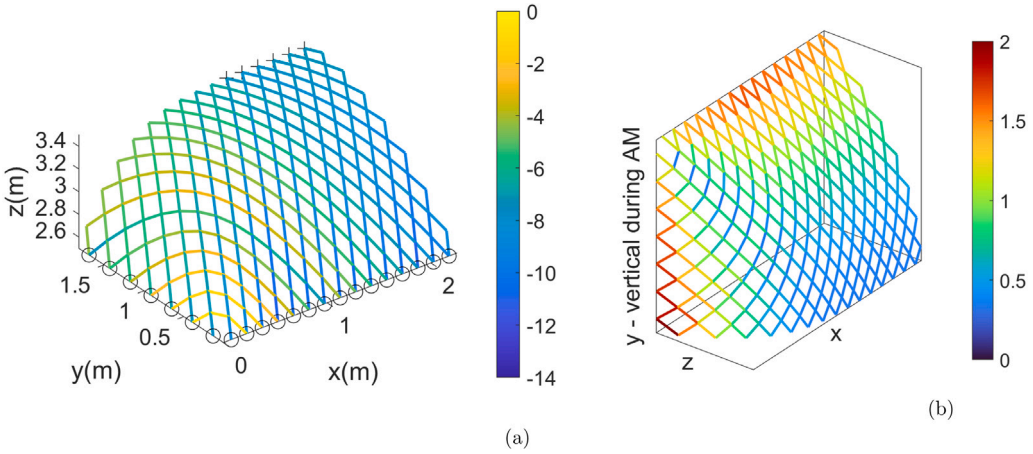

Fig. 5. Example 1. Optimal design using as objective function f_r, disregarding overhang constraints: spatial network and element forces in N (a); orientation during AM with map of $\tan\alpha_{iy}$ squared (b).

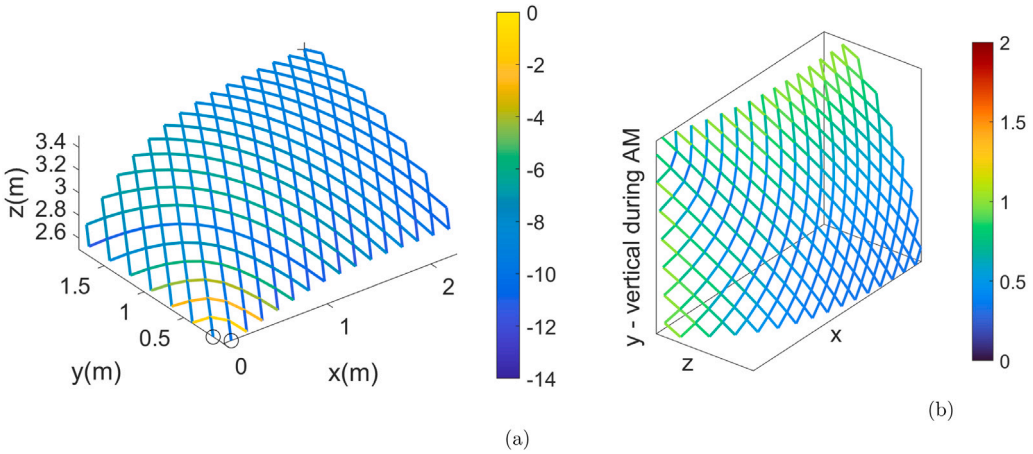

Fig. 6. Example 1. Optimal design using as objective function f_r, with overhang constraints: optimal spatial network and element forces in N (a); feasibility with respect to overhang constraints (b).

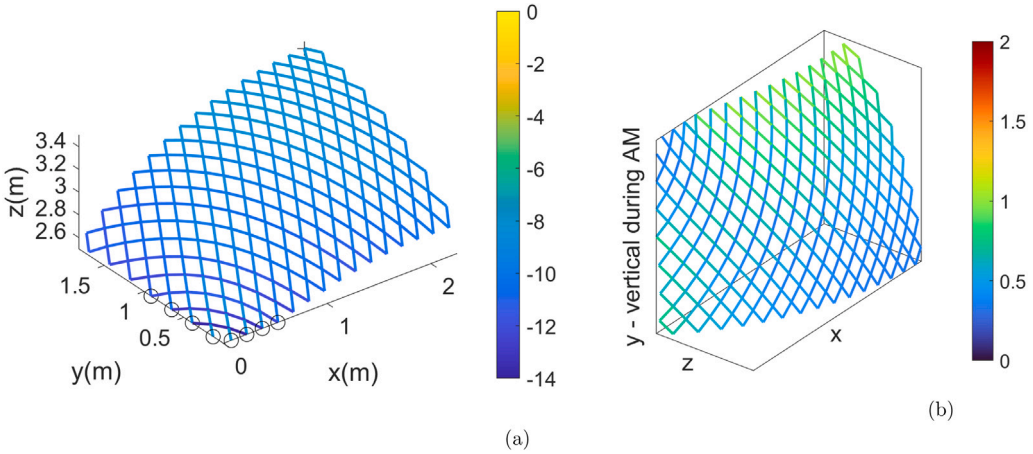

Fig. 7. Example 1. Optimal design using as objective function f_s, with overhang constraints: optimal spatial network and element forces in N (a); feasibility with respect to overhang constraints (b).

Fig. 3(b). This means that, for the same value of $-s_i/s_{c\,i}$, larger forces can be reached in shorter bars. While both networks of minimum thrust are characterized by high variability in the magnitude of the forces, a smaller range is reported for the stress-based solution in Fig. 7(a). This affects the shape of the optimal solution, as well as the overall length, i.e. the weight, since the stress-based solution is the lightest

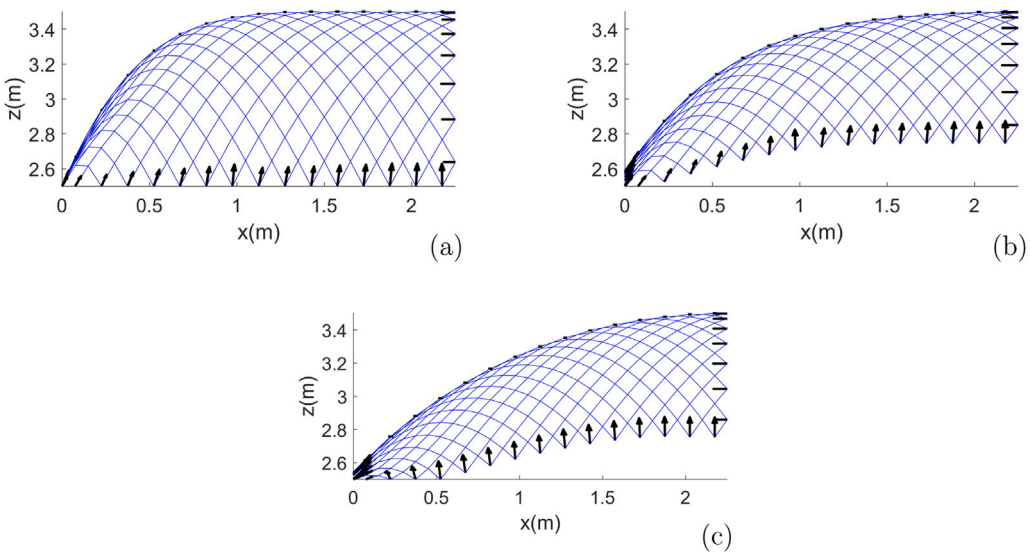

Fig. 8. Example 1. Funicular networks and reactions, using as objective function: f_r, without overhang constraints (a); f_r, with overhang constraints (b); f_s, with overhang constraints (c).

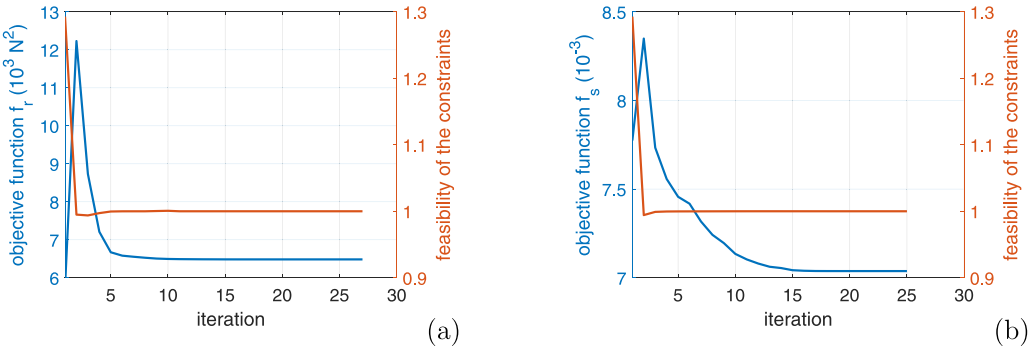

Fig. 9. Example 1. History plot of the objective function and of the feasibility of the constraints, for: f_r, with overhang constraints (a); f_s, with overhang constraints (b). Initialization with $\overline{q}_k = -50\,\mathrm{N/m}\ \forall k$, and $z_{fh} = 3\,\mathrm{m}\ \forall h$.

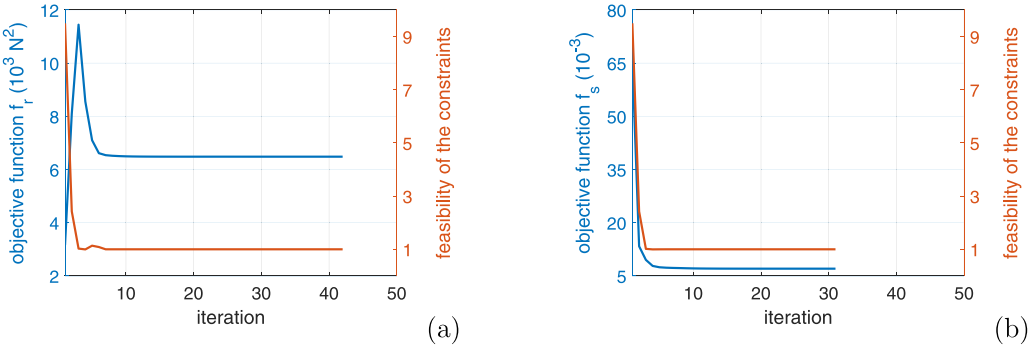

Fig. 10. Example 1. History plot of the objective function and of the feasibility of the constraints, for: f_r, with overhang constraints (a); f_s, with overhang constraints (b). Initialization with $\overline{q}_k = (k-50)\,\mathrm{N/m}$, for $k = 1,\ldots,m-r$, and $z_{fh} = (3.5 - h/n_h)\,\mathrm{m}$, for $h = 1,\ldots,n_h$.

one. According to the evaluation of f_r at convergence, an increase in the value of the horizontal components of the reactions is found.

Lateral views of the three networks are presented in Fig. 8, along with vectorial plots of the reactions. Figs. 8(a) and (b) refer to minimum thrust solutions, without and with overhang constraints, respectively. In Fig. 8(c), the stress-based layout (with overhang constraints) is represented. Comparing overhang-constrained layouts, major differences arise in the vicinity of the fully restrained corner.

The fourth row in Table 1 refers to the solution of a design problem in which the dependence of the critical stress in compression on the printing direction is disregarded. This means that s_{ci} has the same value in each bar, as evaluated for $\alpha_{iy} = 0°$, see Eq. (5). With respect to the design achieved taking into full account the variability of s_{ci} with the printing direction, a negligible variation may be reported in terms of shape. As expected, the maximum value of the ratio $-s_i/s_{ci}$ remarkably decreases (−25%). Minor variations are reported in terms of

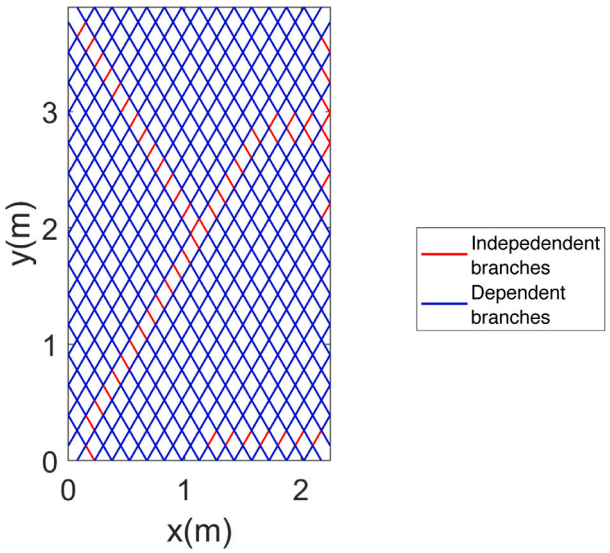

Fig. 11. Example 2 and 3. Fixed plan geometry for the generation of optimal spatial networks. Independent branches are marked in red. (For interpretation of the references to color in this figure legend, the reader is referred to the web version of this article.)

Table 1
Data summary for Example 1. The symbol (*) refers to a design problem in which it is assumed that $s_{c\,i} = s_{c\,i}(\alpha_{i\,y} = 0°)\ \forall i$.

Fig.	O.f. type	f_r (N^2)	f_s $\max\left(-\frac{s_i}{s_{c\,i}}\right)$	$\min s_i$ (N)	Overhang $\max\left(\frac{\tan\alpha_i}{\tan\alpha_{max}}\right)^2$	Length (m)
5	f_r	3759	$9.4\ 10^{-3}$	−11.05	1.98	72.46
6	f_r	6483	$8.1\ 10^{-3}$	−11.49	1.00	68.19
7	f_s	8630	$7.0\ 10^{-3}$	−13.81	1.00	67.36
	f_s(*)	8465	$5.2\ 10^{-3}$	−13.51	1.00	67.41

the maximum compressive force and of the value of f_r at convergence (less than 3%).

Fig. 9 shows history plots of the objective function and of the feasibility of the local enforcements for the optimization of the overhang-constrained layouts in Figs. 6 and 7. The latter quantity accounts both for the ratios z_j/z_j^{min} and z_j/z_j^{max} and for the left hand side of the enforcements in Eq. (12)d. In the very first steps the algorithm has to reach the feasible design domain starting from an unfeasible point. Indeed, the selected starting point is such that some constraints are violated (being the feasibility larger than one). In the subsequent iterations, optimal values of the minimization unknowns are smoothly derived. Both the minimum thrust solution and the stress-based design require less than 30 iterations to meet convergence with the expected tolerance (less than 10^{-3} in terms of relative variation between the value of each parameter in two subsequent iterations).

The problems in Eqs. (12) and (16) are highly non-convex, implying that convergence to a global optimum cannot be guaranteed [21]. Different initial guesses may be conveniently adopted to investigate more on the optimality of the achieved layouts. In Fig. 10, history plots refer to the solution of the overhang-constrained problems, using the starting guess $\overline{q}_k = (k - 50)\,\mathrm{N/m}$, for $k = 1, \ldots, m - r$, with $z_{f\,h} = (3.5 - h/n_h)\,\mathrm{m}$, for $h = 1, \ldots, n_h$. The optimal shapes and the values of the objective function at convergence are those previously retrieved. However, this does not exclude the arising of a better solution. Smooth convergence is observed, notwithstanding the larger variations reported both in terms of objective function and of the feasibility of the local enforcements.

5.2. Example 2

A rectangular bay with size $d_x = 2.25\,\mathrm{m} \times d_y = 3.90\,\mathrm{m}$ is addressed, see Fig. 11. The nodes located along the perimeter are restrained in the three directions ($n_f = 60$). According to the Gauss–Jordan elimination performed on the system of equations governing the equilibrium in the x and y axes, the dependent force densities are $r = 840$, out of $m = 896$ branches. The branches corresponding to the set of $m - r = 56$ independent force densities used in the simulations are depicted in red in the picture. Hence, the optimization problem is formulated in terms of 116 optimization unknowns (56 force densities and 60 vertical coordinates of the restrained nodes). A set of $2 \cdot n = 840$ constraints is used to enforce the feasible bounds for the height of the unrestrained nodes. As in the previous example, the lower limit is set to $z^{min} = 2.5\,\mathrm{m}$, whereas the upper one reads $z^{max} = 3.5\,\mathrm{m}$, respectively. Side constraints governing the height of the fully restrained edge enforce the following upper and lower bounds (in m):

$$z_{f\,h}^{min} = \max\left(2.5, 2.75 - 2(x/d_x - 1/2)(y/d_y - 1/2)\right),$$
$$z_{f\,h}^{max} = \min\left(3.5, 3.25 - 2(x/d_x - 1/2)(y/d_y - 1/2)\right).$$

Table 2
Data summary for Example 2. The symbol (*) refers to a design problem in which it is assumed that $s_{Y\,i} = s_{Y\,i}(\alpha_{i\,y} = 0°)\ \forall i$.

Fig.	O.f. type	f_r (N^2)	f_s $\max\left(\frac{s_i}{s_{Y\,i}}\right)$	$\max s_i$ (N)	Overhang $\max\left(\frac{\tan\alpha_i}{\tan\alpha_{max}}\right)^2$	Length (m)
12(a)	f_r	2997	$2.4\ 10^{-3}$	14.39	4.43	153.31
12(b)	f_r	5367	$2.7\ 10^{-3}$	15.80	1.00	143.50
13	f_s	7556	$1.6\ 10^{-3}$	9.29	1.00	143.39
	f_s(*)	7551	$1.4\ 10^{-3}$	9.28	1.00	143.40

Optimal funicular networks are sought implementing side constraints $\overline{q}_k \geq 0\ \forall k$. The minimization algorithm is initialized with $\overline{q}_k = 50\,\mathrm{N/m}\ \forall k$, and $z_{f\,h} = (z_{f\,h}^{min} + z_{f\,h}^{max})/2\ \forall h$.

The solution achieved when seeking for minimum thrust networks while disregarding the overhang constraints of Eq. (12d) is represented in Fig. 12(a). All the nodes along the perimeter have height equal to the upper bound of the admissible interval, whereas nodes along the diagonal connecting the lower corners of the spatial networks match the minimum height allowed. The largest tensile forces are found along the members connecting the higher corners of the spatial networks. Ties parallel to this direction undergo forces that decrease rapidly with distance from the diagonal of the bay. Forces are much lower in the branches having different orientation in the diamond pattern. A data summary is reported in the first row of Table 2. The maximum tensile force among all s_i reads 14.39 N, whereas the maximum value of the ratio $s_i/s_{Y\,i}$ (force to yielding force in each branch) is $2.4 \cdot 10^{-3}$. Again, the most favorable setting to build the designed gridshell (by parts or as a whole) consists in aligning the y axis with the vertical direction during the AM process. However, the maximum value of the squared ratio $(\tan\alpha_{i\,y}/\tan\alpha_{max})^2$ reads 4.43 for this layout. Indeed, the build angle of many bars, especially those located around the lower corners of the bay, exceed the prescribed limit $\alpha_{max} = 45°$ by far.

To control build angles $\alpha_{i\,y}$, an optimization run is performed searching for networks of minimum thrust and accounting for the overhang constraints in Eq. (12d). An additional set of $m = 896$ local enforcements is handled within the multi-constrained formulation. The optimal result is represented in Fig. 12(b), see second row of Table 2 for some relevant data. Full feasibility with respect to overhang constraints is recovered at the cost of an increase in the value of the objective function f_r at convergence, and a minor growth in the maximum tensile force read in the branches of the network. In the achieved spatial network, only a few nodes have height equal to the upper bound or the lower one. The network is shallower than the previous one and tensile forces are generally higher also in the direction parallel to the diagonal of the bay connecting its lower corners.

A further investigation is performed using the stress-based approach, with objective function $f = f_s$ and overhang constraints for

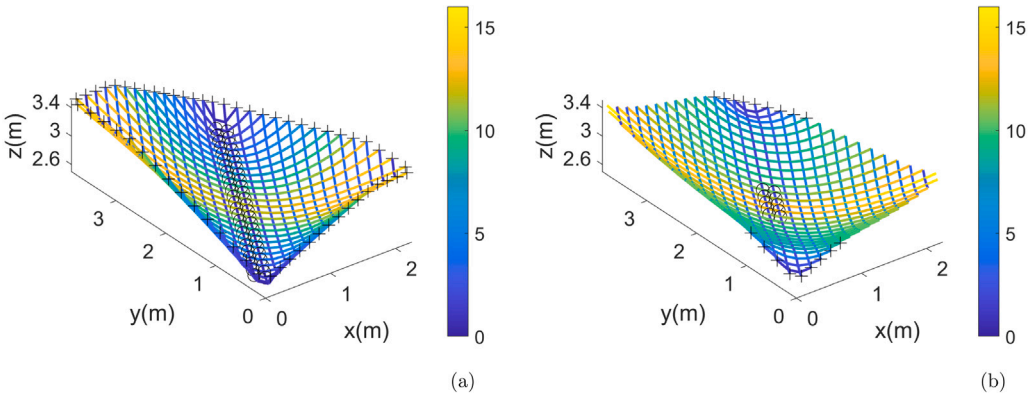

Fig. 12. Example 2. Optimal spatial networks and element forces in N, using as objective function: f_r, disregarding overhang constraints (a); f_r, with overhang constraints (b).

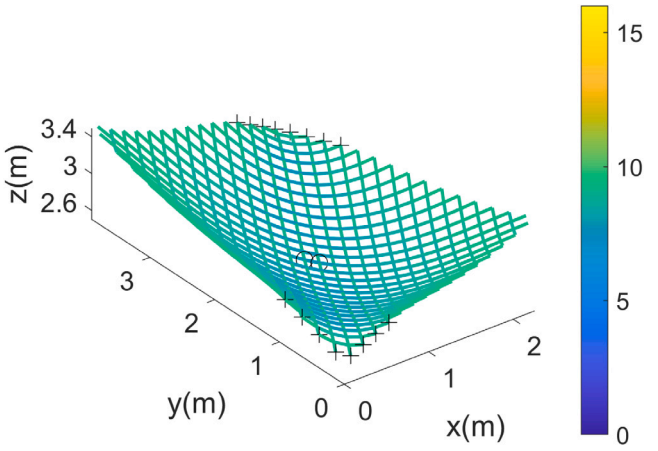

Fig. 13. Example 2. Optimal spatial network and element forces in N, using as objective function f_s, with overhang constraints.

the build angles α_{iy}. This means minimizing the maximum value of the ratio s_i/s_{Yi} over the branches constituting the spatial network. The optimal result is represented in Fig. 13, whereas some relevant data may be retrieved in the third row of Table 2. Full feasibility with respect to the overhang constraints is achieved. As already seen for the optimal solution in Fig. 12(b), only a few nodes have their z coordinate that equals the allowed lower or upper bound. When reviewing the stress-based anti-funicular design in Fig. 7(a), the limited range of variation of the compressive forces in the members of the network was pointed point. A peculiar feature of the stress-based funicular solution of Fig. 13 is the almost homogeneous distribution of the tensile forces in the branches. Indeed, the stress-based design outperforms the layouts of minimum thrust both in terms of maximum value of s_i/s_{Yi}, with $s_{Yi}(\alpha)$, and in terms of largest s_i. With respect to the design for minimum thrust with overhang constraints, the decrease is around 40% for both quantities, with a similar increase for f_r evaluated at convergence. The length (weight) of the stress-based solution is almost equivalent to that reported for the minimum thrust solution with overhang constraints.

The fourth row in Table 2 refers to the solution of a design problem in which the dependence of the yielding stress on the printing angle is disregarded, assuming $s_{Yi} = s_{Yi}(\alpha_{iy} = 0°)$ for all the branches in the network. With respect to the solution achieved taking into full account the dependence of s_{Yi} on the printing direction, the only difference is that affecting the maximum value of the ratio s_i/s_{Yi}. Indeed, both the shape and the force distribution in the optimal network are the same as those represented in Fig. 13.

5.3. Example 3

The grid already considered in the previous example, see Fig. 11, is addressed. The same boundary conditions apply. With the aim of generating a saddle-like shape with members in tension and compression, the restrained node along the perimeter of the bay have a fixed height according to the following equation (in m):

$$z_{fh} = 3 - 2(x/d_x - 1/2)(y/d_y - 1/2).$$

A variation of ± 0.25 m is allowed to the unrestrained nodes, with respect to the above hyperbolic paraboloid, that means (in m):

$$z_j^{min} = 2.75 - 2(x/d_x - 1/2)(y/d_y - 1/2),$$
$$z_j^{max} = 3.25 - 2(x/d_x - 1/2)(y/d_y - 1/2).$$

All the optimizations problems in this section are formulated in terms of the set of the independent force densities only, which are the same used in the previous example.

At first, minimum thrust layouts are investigated. In Fig. 14(a), the design without overhang constraints is reported, whereas Fig. 14(b) concerns the one accounting for limitations on the build angle α_{iy}. Relevant data are presented in the first and second row of Table 3, respectively. In both cases, a few points in the network have height equal to the allowed minimum value, whereas no node is located at the upper bound. The maximum value of the tensile forces s_i is almost the same in the two cases, as well as the largest value of the element ratio s_i/s_{Yi}, where it is remarked that the yielding force s_{Yi} depends on the build angle. Overhang constraints have a major effect on the orientation of the compressive members located next to the lower corners of the spatial network. For the overhang-constrained solution, a decrease of around 20% is reported in terms of the maximum value of the compressive force in the network, whereas the largest value of the element ratio $-s_i/s_{ci}$ is 60% less. It must be remarked that the critical compressive force s_{ci} increases when reducing the build angle of the re-oriented members. This is mainly due to the reduced length of the bars, but also to the larger value of $\sigma_Y(\alpha_{iy})$ and smaller lack-of-straightness $e(\alpha_{iy})$, see Eq. (5). It is finally pointed out that the increase in the value of the objective function f_r read at convergence is quite low, compared to the solution without overhang constraint.

The optimal stress-based layout found using $f = f_s$ (with overhang constraints) is reported in Fig. 15(a). Some relevant data are given in the third row of Table 3. The shape of the network is remarkably different from the layouts found when seeking for minimum thrust. A peculiar feature of the stress-based layout is that it exhibits the same maximum value among the element ratios $-s_i/s_{ci}$ and s_i/s_{Yi}. Compared to the overhang-constrained network of Fig. 14(b), a decrease of around 20% is reported both in the magnitude of the maximum force (in tension) and in the magnitude of the minimum force (in compression) read in the branches of the spatial network. Due to the slenderness of

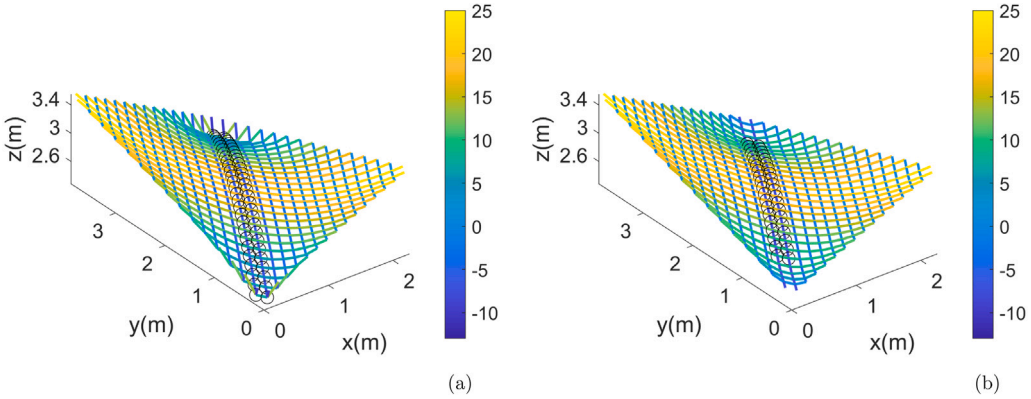

Fig. 14. Example 3. Optimal spatial networks and element forces in N, using as objective function: f_r, disregarding overhang constraints (a); f_r, with overhang constraints (b).

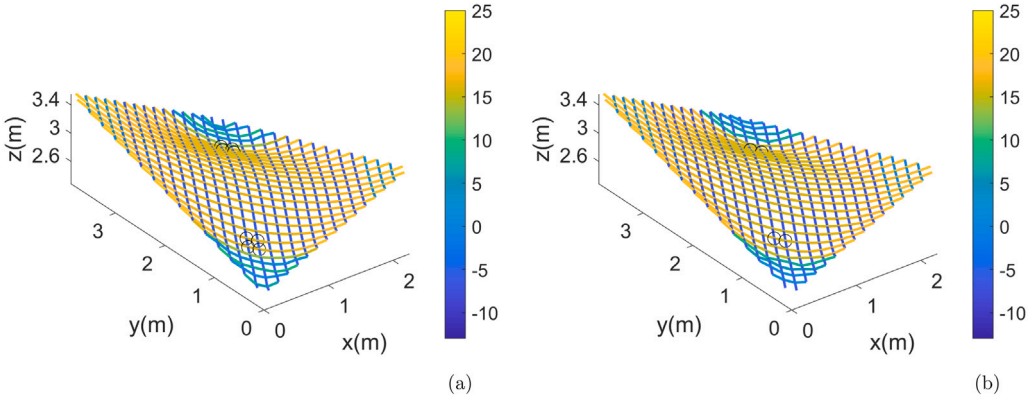

Fig. 15. Example 3. Optimal spatial networks and element forces in N, using as objective function f_s, with overhang constraints: considering the dependence of s_{ci} and s_{Yi} on the build angle (a); assuming $s_{ci} = s_{ci}(\alpha_{iy} = 0°)$ and $s_{Yi} = s_{Yi}(\alpha_{iy} = 0°)$, $\forall i$ (b).

the bars, which range from 100 to 123 in the stress-based solution, the ratio $|\max s_i / \min s_i|$ is around 3, see also Fig. 3(b).

The optimal solution of the overhang-constrained stress-based problem, when assuming that s_{ci} and s_{Yi} are those computed for $\alpha_{iy} = 0°$ in all the branches of the network, is given in Fig. 15(b). With respect to the optimal network represented in Fig. 15(a), there are some differences in the orientation of the bars that are located around the lower corners of the bay. Disregarding the dependence of the mechanical parameters on the printing angle, the maximum value of the ratio $-s_i/s_{ci}$, which is still equal to that of s_i/s_{Yi}, is 18% lower. In this case, a 10% increase is reported in the magnitude of the maximum compressive force, whereas only a minor variation (less than 3%) affects the maximum tensile force, see the fourth row in Table 3. When $-s_i/s_{ci}$ and s_i/s_{Yi} are evaluated considering the forces s_i in the network of Fig. 15(b), along with s_{ci} and s_{Yi} computed for the relevant distribution of α_{iy}, their maximum value reads $3.78 \cdot 10^{-3}$ and $2.8 \cdot 10^{-3}$, respectively. Hence, disregarding the dependence of s_{ci} and s_{Yi} on α_{iy} in the optimization, costs around 10% in terms of f_s.

A further set of numerical simulations is performed considering diamond-like gridshells having bars whose length, measured in the (fixed) projection onto the horizontal plane, is halved, i.e. $l_{xy} = 0.15/2 = 0.075$ m. The reference load (roughly approximating the self-weight) is scaled by the same factor, meaning that nodal forces equal to 0.5 N are applied along the z axis all over the network. The whole geometry is reduced by one-half, affecting d_x, d_y, z_{fh}, z_j^{min} and z_j^{max}. As expected, the overhang-constrained optimization for minimum thrust provides the same shape represented in Fig. 14(b), see Fig. 16(a). The only difference stands in the magnitude of the forces, which is halved, see also the fifth row in Table 3. In Fig. 16(b), the optimal stress-based layout (considering the dependence of the mechanical parameters on the printing angle) is depicted, whereas relevant data are reported in the last row of the table. Again, the maximum value of the element ratios $-s_i/s_{ci}$ matches that of s_i/s_{Yi}. However, the optimal shape is quite different with respect to that represented in Fig. 15(a), and the ratio $|\max s_i / \min s_i|$ is around 1.5. Indeed, the slenderness of the bars ranges, in this case, from 50 to 62.

Since the slenderness of the bars is mainly related to the value of l_{xy}, it must be remarked that the spacing of the adopted grid has a noticeable impact on the optimal solution when designing networks with element in tension and compression and accounting for stress considerations.

5.4. Example 4

In this example, a spatial network with repetitive structure is addressed. The gridshell, for instance a lightweight roof, has vertical supports which are located in a diamond pattern with side $d_l = \sqrt{d_x^2 + d_y^2} = 4.50$ m, being $d_x = 2.25$ m and $d_y = 3.90$ m, see Fig. 17(a). The grid in Fig. 17(b) is the fixed plan projection of the representative portion of the network. The length of the bars, measured in the horizontal plane, is 0.15 m or 0.075 m. The seven nodes of the grid which are closest to the corner with coordinates $x = d_x = 2.25$ m, $y = 0$ m are fully restrained, as well as the seven nodes nearest to the corner at $x = 0$ m, $y = d_y = 3.90$ m. For the former set of nodes, the height is equal to 2.5 m. For the latter, the elevation may vary between $z_{fh}^{min} = 3.75$ m and $z_{fh}^{max} = 4.25$ m. Symmetry boundary conditions are enforced all over the perimeter: nodes lying along sides of the rectangular bay which are parallel to the x axis are restrained in the y direction, whereas nodes on sides parallel to the y axis are restrained in the x direction. A minimum slope of 4% is enforced by prescribing (in m):

$$z_j^{min} = 2.5 + 0.04 d_y (1 - x/d_x + y/d_y),$$

Table 3
Data summary for Example 3. The symbol (*) refers to a design problem in which it is assumed that $s_{c\,i} = s_{c\,i}(\alpha_{i\,y} = 0°)$ and $s_{Y\,i} = s_{Y\,i}(\alpha_{i\,y} = 0°)$, $\forall i$.

Fig.	O.f. type	f_r (N^2)	f_s max $\left(\frac{-s_i}{s_{c\,i}}\right)$	max $\left(\frac{s_i}{s_{Y\,i}}\right)$	min s_i (N)	max s_i (N)	Overhang max $\left(\frac{\tan\alpha_i}{\tan\alpha_{max}}\right)^2$	Length (m)
14(a)	f_r	8987	11.4 10^{-3}	4.1 10^{-3}	−10.20	24.02	4.25	142.62
14(b)	f_r	9322	4.5 10^{-3}	4.1 10^{-3}	−8.30	24.20	1.00	140.07
15(a)	f_s	12405	3.4 10^{-3}	3.4 10^{-3}	−6.57	19.68	1.00	139.62
15(b)	f_s(*)	12220	2.8 10^{-3}	2.8 10^{-3}	−7.29	19.24	1.00	139.52
16(a)	f_r	2331	1.0 10^{-3}	2.1 10^{-3}	−4.15	12.10	1.00	70.04
16(b)	f_s	4891	1.5 10^{-3}	1.5 10^{-3}	−6.38	9.06	1.00	69.07

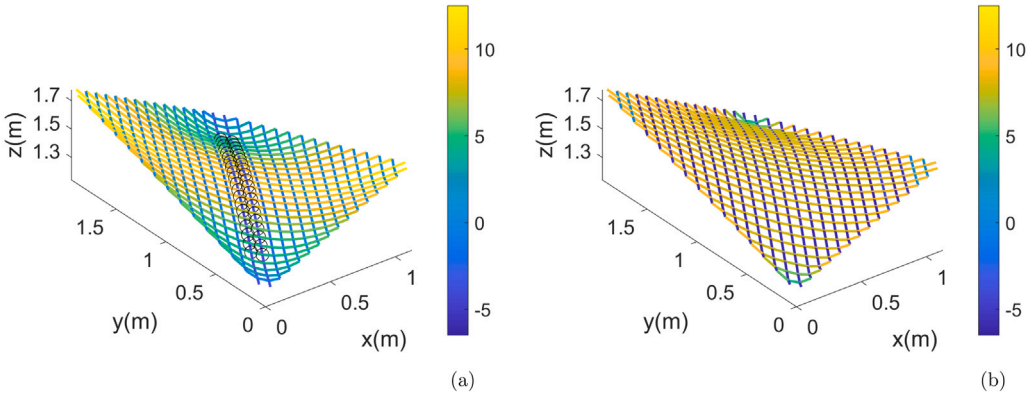

Fig. 16. Example 3. Optimal spatial networks and element forces in N for $l_{xy} = 0.075$ m, using as objective function: f_r, with overhang constraints (a); f_s, with overhang constraints (b).

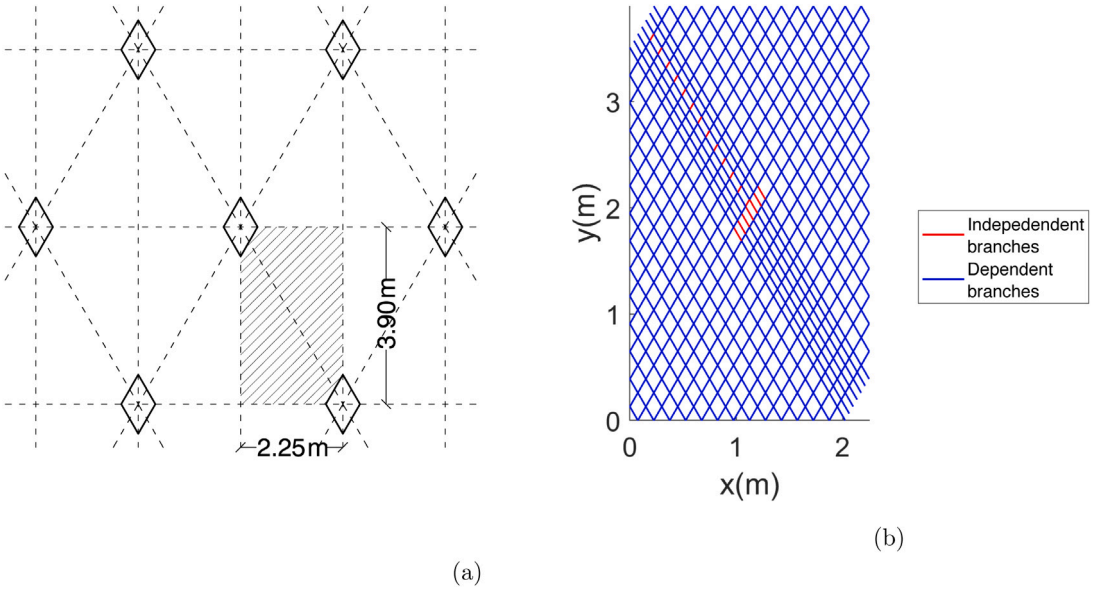

Fig. 17. Example 4. Generation of optimal spatial networks with repetitive structure: general plan (a); fixed plan geometry of a representative portion, with independent branches marked in red (b). (For interpretation of the references to color in this figure legend, the reader is referred to the web version of this article.)

whereas $z_j^{max} = 4.25$ m for all the unrestrained nodes. A distributed load with magnitude 1.35 kN/m^2 is addressed, consisting of nodal forces acting along the z axis. The intensity takes values in the range 13.15–26.30 N, depending on the tributary area of each node. In this example, the number of dependent force densities is $r = 1027$ (out of $m = 1047$ branches). Hence, the number of minimization unknowns reads $m-r+n_f = 27$. Optimal funicular networks are sought implementing side constraints $\bar{q}_k \geq 0\ \forall k$. The minimization algorithm is initialized with $\bar{q}_k = 50$ kN/m $\forall k$, and $z_{f\,h} = (z_{f\,h}^{min} + z_{f\,h}^{max})/2\ \forall h$.

In the optimal design, limitations on the build angle $\alpha_{i\,y}$ are accounted for. The minimum thrust layout is represented in Fig. 18(a). Due to overhang constraints, the top nodes of the network are located below the maximum allowed height. Only for a few nodes, the elevation is equal to the minimum allowed value. The branches located along the diagonal lines that connect the two sets of vertical supports are those subjected to the largest stresses. Relevant data are given in the first row of Table 4. The maximum value among the tensile forces is 3.77 kN, corresponding to a ratio $s_i/s_{Y\,i}$ equal to 0.64. A shallower spatial network is found when using f_s as objective function, see Fig. 18(b). Two of the top nodes of the network are located at the minimum allowed height, as well as a few nodes next to the lower support region. In this design, highly-stressed branches are found along

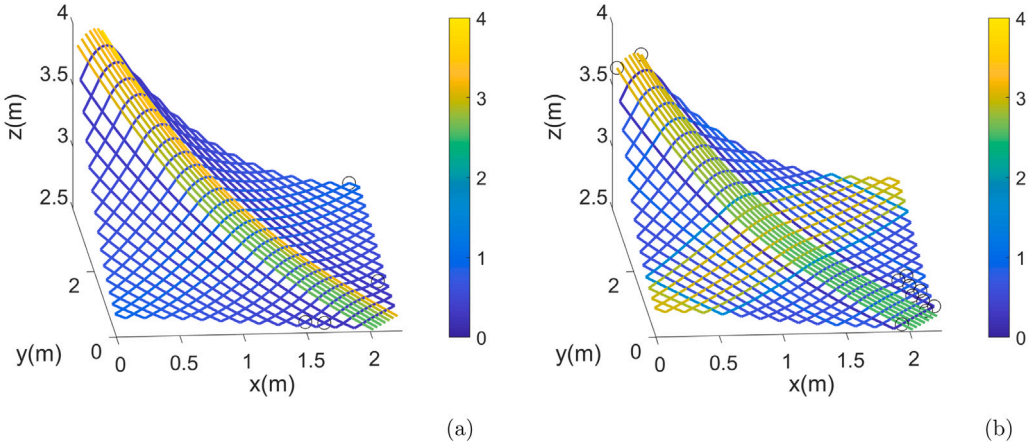

Fig. 18. Example 4. Optimal spatial networks and element forces in kN, using as objective function: f_r, with overhang constraints (a); f_s, with overhang constraints (b).

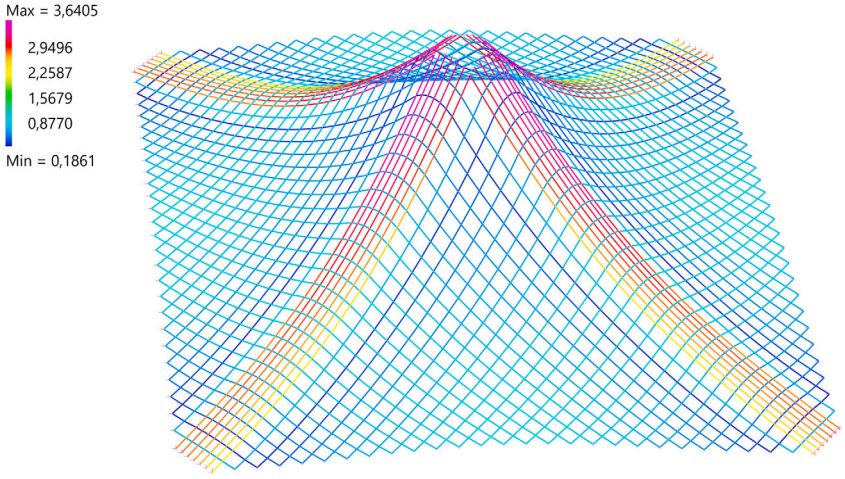

Fig. 19. Example 4. Element forces in kN computed for the assemblage of four gridshells of the type in Fig. 18(a) using finite element analysis.

both diagonals of the rectangular bay. Relevant data are reported in the second row of Table 4. A 18% decrease in terms of maximum tensile force, corresponding to a ratio s_i/s_{Yi} equal to 0.53, is found. This has the cost of a remarkable increase in terms of horizontal reactions, see f_r.

It must be remarked that the proposed design approach is based on equilibrium only, meaning that the elastic response of the bars is not accounted for within the optimization procedure. A linear finite element analysis of the assemblage of four repetitive gridshells of the type in Fig. 18(a) has been performed, using a commercial software [59]. Beam elements have been used, adopting the same elastic modulus for all the bars, i.e. the value found in Eq. (1a) for $\alpha_{iy} = 45°$. The investigated portion of the network spans an area with size 4.50 m $\times$ $d_y = 7.80$ m, including five vertically supported regions. Symmetry boundary conditions are enforced all over the perimeter. A map of the axial forces computed in the branches of the network for the load case addressed in the design phase is given in Fig. 19. The maximum value of the forces is only 3% less than that read in the results of the force density method reported in Fig. 18(a). Negligible values of the bending moment are found ($< 10^{-4}$ kNm), thus confirming the achievement of a funicular solution. The maximum value of the nodal displacements in the vertical direction is less than 1.5 cm.

Table 4
Data summary for Example 4.

Fig.	O.f. type	f_r (kN^2)	f_s $\max\left(\frac{s_i}{s_{Yi}}\right)$	$\max s_i$ (kN)	overhang $\max\left(\frac{\tan\alpha_i}{\tan\alpha_{max}}\right)^2$	Length (m)
18(a)	f_r	144	0.64	3.77	1.00	150.86
18(b)	f_s	348	0.53	3.10	1.00	149.16

6. Conclusions and future research

In this contribution, multi-constrained formulations for the optimal design of Wire-and-Arc Additive Manufactured gridshells have been dealt with. Relying upon experimental data concerning bars built using dot-by-dot WAAM with 304L stainless steel, a material characterization has been preliminary performed. This in view of the formulation of optimization problems accounting for features peculiar to the considered metal printing technique.

The orientation of the bar growth with respect to the vertical direction, i.e. the build angle, affects the mechanical properties of the printed bars. Smooth interpolations have been proposed to approximate the values of the elastic modulus and of the yielding stress of the printed material, along with the lack-of-straightness of the bars, depending on the build angle. The Perry–Robertson capacity formula has been used to predict failure in compression, interpolating between yielding of very stud bars to elastic buckling of very slender ones, while taking into account the effect of the measured eccentricity. A good agreement has been found between the computed critical stress and the experimental results for bars with different slenderness, printed with build angle equal to zero. An extension of this formula has been proposed for build angles in the range 0°–45°.

Spatial networks acted upon by axial forces only have been investigated, using the force density method to handle the equilibrium of the nodes. Gridshells with fixed plan projection have been dealt with, formulating optimization problems whose unknowns are any set of independent force densities, along with the height of the nodes having restraints in the vertical direction. Local constraints have been used to prescribe an upper and a lower bound to the height of each node in the spatial network, and to control the build angle of each element. A maximum overhang of 45° has been enforced, in agreement with the outcome of the experimental investigations. Two objective functions have been considered, seeking for networks of minimum thrust, either implementing a stress-based design. In the latter case, the maximum value of the ratio axial force to yielding/critical force over the elements has been adopted as objective function.

Numerical simulations have been performed considering anti-funicular networks, funicular ones, and gridshells with a saddle-like shape. In all the cases, full feasibility of the enforced sets of constraints is reported. Dealing with networks of minimum thrust, overhang constraints have been found to impact both the optimal shape of the structure and the magnitude of the horizontal reactions. A more homogeneous distribution of the forces has been observed in stress-based layouts, characterized by smaller ranges of variation of tensile and compressive forces. This implies a slight reduction in terms of the overall weight, but comes with an increase in the magnitude of the horizontal reactions. When dealing with saddle-like gridshells, the same maximum value has been found, in stress-based layouts, for the ratios tensile force/yielding force and compressive force/critical force. Due to the dependence of the critical force on the bar slenderness, the size of the grid remarkably affects the results, both in terms of optimal layout and stress regime.

The proposed approach may be used to investigate the optimal form of patterns of WAAM-printed bars addressing different applications. These include: (i) self-supporting gridshells which are mainly created for architectural purposes and may be printed as a whole, while respecting overhang constraints; (ii) loaded spatial networks in which the assemblage of smaller parts is implemented to overcome manufacturing limitations. Following the implementation for ribbed spatial networks presented in [51], gridshells made of multiple layers could be conveniently handled. Reference is also made to the extension of the proposed methodology to the optimal design of other structural components made of WAAM-printed bars, see in particular the diagrid column in [17].

In its current version, the method is limited to equilibrium considerations. A linear finite element analysis has been preliminary performed on one of the optimal layouts, finding good agreement with results from the considered funicular solution. The achieved layouts should be assessed using geometric non-linear analyses up to the applied load. Especially in the case of anti-funicular networks, it must be remarked that global stability has not been considered, at this stage, in the implemented design procedure. The ongoing research is mainly devoted to the extension of the proposed approach to account for global buckling. Reference is made in particular to the work by [60], where stability is discussed within the framework of truss layout optimization.

CRediT authorship contribution statement

Matteo Bruggi: Conceptualization, Methodology, Software. **Vittoria Laghi:** Formal analysis, Investigation, Data curation. **Tomaso Trombetti:** Conceptualization, Resources.

Declaration of competing interest

The authors declare that they have no known competing financial interests or personal relationships that could have appeared to influence the work reported in this paper.

Data availability

Data will be made available on request.

References

[1] Sauerwein M, Doubrovski E, Balkenende R, Bakker C. Exploring the potential of additive manufacturing for product design in a circular economy. J Clean Prod 2019;226:1138–49.
[2] Wu P, Wang J, Wang X. A critical review of the use of 3-D printing in the construction industry. Autom Constr 2016;68:21–31.
[3] Boje C, Guerriero A, Kubicki S, Rezgui Y. Towards a semantic construction digital twin: Directions for future research. Autom Constr 2020;114.
[4] Buchanan C, Gardner L. Metal 3D printing in construction: A review of methods, research, applications, opportunities and challenges. Eng Struct 2019;180:332–48.
[5] Paolini A, Kollmannsberger S, Rank E. Additive manufacturing in construction: A review on processes, applications, and digital planning methods. Addit Manuf 2019;30.
[6] Rodrigues TA, Duarte V, Miranda RM, Santos TG, Oliveira JP. Current status and perspectives on wire and arc additive manufacturing (WAAM). Mater 2019;12(7).
[7] Kanyilmaz A, Demir AG, Chierici M, Berto F, Gardner L, Kandukuri SY, et al. Role of metal 3D printing to increase quality and resource-efficiency in the construction sector. Addit Manuf 2022;50.
[8] Priarone PC, Pagone E, Martina F, Catalano AR, Settineri L. Multi-criteria environmental and economic impact assessment of wire arc additive manufacturing. CIRP Ann 2020;69(1):37–40.
[9] Gordon JV, Haden CV, Nied HF, Vinci RP, Harlow DG. Fatigue crack growth anisotropy, texture and residual stress in austenitic steel made by wire and arc additive manufacturing. Mater Sci Eng A 2018;724:431–8.
[10] Wu W, Xue J, Wang L, Zhang Z, Hu Y, Dong C. Forming process, microstructure, and mechanical properties of thin-walled 316L stainless steel using speed-cold-welding additive manufacturing. Metals 2019;9(1).
[11] Feucht T, Lange J. 3-D-printing with steel: additive manufacturing of connection elements and beam reinforcements. In: IABSE symposium, Guimaraes 2019: Towards a resilient built environment risk and asset management - Report. 2019.
[12] Gardner L, Kyvelou P, Herbert G, Buchanan C. Testing and initial verification of the world's first metal 3D printed bridge. J Constr Steel Res 2020;172.
[13] Kyvelou P, Slack H, Daskalaki Mountanou D, Wadee MA, Britton TB, Buchanan C, et al. Mechanical and microstructural testing of wire and arc additively manufactured sheet material. Mater Des 2020;192.
[14] Joosten S. Printing a stainless steel bridge - An exploration of structural properties of stainless steel additive manufactures for civil engineering purposes. The Netherlands: Delft University of Technology; 2015.
[15] Müller J, Grabowski M, Müller C, Hensel J, Unglaub J, Thiele K, et al. Design and parameter identification of wire and arc additively manufactured (WAAM) steel bars for use in construction. Metals 2019;9(7).
[16] Silvestru V-, Ariza I, Vienne J, Michel L, Aguilar Sanchez AM, Angst U, et al. Performance under tensile loading of point-by-point wire and arc additively manufactured steel bars for structural components. Mater Des 2021;205.
[17] Laghi V, Palermo M, Gasparini G, Trombetti T. Computational design and manufacturing of a half-scaled 3D-printed stainless steel diagrid column. Addit Manuf 2020;36.
[18] Carpo M. The digital turn in architecture 1992-2012. John Wiley and Sons; 2013.
[19] Adriaenssens S, Block P, Veenendaal D, Williams C. Shell structures for architecture: form finding and optimization. Routledge; 2014.
[20] Ching E, Carstensen JV. Truss topology optimization of timber-steel structures for reduced embodied carbon design. Eng Struct 2022;252.
[21] Christensen PW, Klarbring A. An introduction to structural optimization. Solid Mech Appl 2008;153:1–220.
[22] Sigmund O, Maute K. Topology optimization approaches: A comparative review. Struct Multidiscip Opt 2013;48(6):1031–55.
[23] Liu J, Gaynor AT, Chen S, Kang Z, Suresh K, Takezawa A, et al. Current and future trends in topology optimization for additive manufacturing. Struct Multidiscip Opt 2018;57(6):2457–83.
[24] Meng L, Zhang W, Quan D, Shi G, Tang L, Hou Y, et al. From topology optimization design to additive manufacturing: Today's success and tomorrow's roadmap. Arch Comput Methods Eng 2019.
[25] Bruggi M, Laghi V, Trombetti T. Simultaneous design of the topology and the build orientation of wire-and-arc additively manufactured structural elements. Comput Struct 2021;242.
[26] Yoon GH. Structural topology optimization of layout and raster angle for additive manufacturing technology with the shadow density filter. Comput Struct 2021;256.
[27] Mishra V, Ayas C, Langelaar M, van Keulen F. Simultaneous topology and deposition direction optimization for wire and arc additive manufacturing. Manuf Let 2022;31:45–51.
[28] Allaire G, Dapogny C, Estevez R, Faure A, Michailidis G. Structural optimization under overhang constraints imposed by additive manufacturing technologies. J Comput Phys 2017;351:295–328.

[29] Guo X, Zhou J, Zhang W, Du Z, Liu C, Liu Y. Self-supporting structure design in additive manufacturing through explicit topology optimization. Comput Methods Appl Mech Engrg 2017;323:27–63.
[30] Pellens J, Lombaert G, Lazarov B, Schevenels M. Combined length scale and overhang angle control in minimum compliance topology optimization for additive manufacturing. Struct Multidiscip Opt 2019;59(6):2005–22.
[31] Bletzinger K-, Wüchner R, Daoud F, Camprubí N. Computational methods for form finding and optimization of shells and membranes. Comput Methods Appl Mech Engrg 2005;194(30–33):3438–52.
[32] Block P, Ochsendorf J. Thrust network analysis: A new methodology for three-dimensional equilibrium. J Int Assoc Shell Spat Struct 2007;48(155):167–73.
[33] Winslow P, Pellegrino S, Sharma SB. Multi-objective optimization of free-form grid structures. Struct Multidiscip Opt 2010;40(1–6):257–69.
[34] Darwich W, Gilbert M, Tyas A. Optimum structure to carry a uniform load between pinned supports. Struct Multidiscip Opt 2010;42(1):33–42.
[35] Veenendaal D, Block P. An overview and comparison of structural form finding methods for general networks. Int J Solids Struct 2012;49(26):3741–53.
[36] Richardson JN, Adriaenssens S, Filomeno Coelho R, Bouillard P. Coupled form-finding and grid optimization approach for single layer grid shells. Eng Struct 2013;52:230–9.
[37] Jiang Y, Zegard T, Baker WF, Paulino GH. Form-finding of grid-shells using the ground structure and potential energy methods: A comparative study and assessment. Struct Multidiscip Opt 2018;57(3):1187–211.
[38] Rombouts J, Lombaert G, De Laet L, Schevenels M. A novel shape optimization approach for strained gridshells: Design and construction of a simply supported gridshell. Eng Struct 2019;192:166–80.
[39] Czubacki R, Lewiński T. Optimal archgrids: A variational setting. Struct Multidiscip Opt 2020;62:1371–93.
[40] Schek H. The force density method for form finding and computation of general networks. Comput Methods Appl Mech Engrg 1974;3(1):115–34.
[41] Block P, Lachauer L. Three-dimensional funicular analysis of masonry vaults. Mech Res Commun 2014;56:53–60.
[42] Cercadillo-García C, Fernández-Cabo JL. Analytical and numerical funicular analysis by means of the parametric force density method. J Appl Res Technol 2016;14(2):108–24.
[43] Liew A, Pagonakis D, Van Mele T, Block P. Load-path optimisation of funicular networks. Meccanica 2018;53(1–2):279–94.
[44] Liew A, Avelino R, Moosavi V, Van Mele T, Block P. Optimising the load path of compression-only thrust networks through independent sets. Struct Multidiscip Opt 2019;60(1):231–44.
[45] Bruggi M. A constrained force density method for the funicular analysis and design of arches, domes and vaults. Int J Solids Struct 2020;193-194:251–69.
[46] Laghi V, Palermo M, Silvestri S, Gasparini G, Trombetti T. Experimental behaviour of wire-and-arc additively manufactured stainless steel rods. Ce/Papers 2021;4:2387–92.
[47] Laghi V, Palermo M, Tonelli L, Gasparini G, Girelli VA, Ceschini L, et al. Mechanical response of dot-by-dot wire-and-arc additively manufactured 304L stainless steel bars under tensile loading. Constr Build Mater 2022;318.
[48] Dwight JB. Use of Perry formula to represent the new European strut curves. IABSE reports of the working commissions, 1975, p. 23.
[49] Svanberg K. Method of moving asymptotes - A new method for structural optimization. Int J Numer Methods Eng 1987;24(2):359–73.
[50] Krenk S, Høgsberg J. Statics and mechanics of structures. Springer; 2013.
[51] Bruggi M, Lógó BA, Deák Z. Funicular analysis of ribbed masonry vaults: A case study. Int J Archit Herit 2022;16(12):1809–23.
[52] Pellegrino S, Calladine CR. Matrix analysis of statically and kinematically indeterminate frameworks. Int J Solids Struct 1986;22(4):409–28.
[53] Descamps B, Coelho RFilomeno, Ney L, Bouillard P. Multicriteria optimization of lightweight bridge structures with a constrained force density method. Comput Struct 2011;89(3–4):277–84.
[54] Baker WF, Beghini LL, Mazurek A, Carrion J, Beghini A. Maxwell's reciprocal diagrams and discrete Michell frames. Struct Multidiscip Opt 2013;48(2):267–77.
[55] Kundu RD, Li W, Zhang XS. Multimaterial stress-constrained topology optimization with multiple distinct yield criteria. Extrem Mech Lett 2022;54.
[56] Svanberg K. MMA and GCMMA - Two methods for nonlinear optimization. 2007, https://people.kth.se/krille/.
[57] da Silva GA, Aage N, Beck AT, Sigmund O. Three-dimensional manufacturing tolerant topology optimization with hundreds of millions of local stress constraints. Int J Numer Methods Eng 2021;122:548–78.
[58] Giraldo-Londoño O, Paulino GH. PolyStress: A matlab implementation for local stress-constrained topology optimization using the augmented Lagrangian method. Struct Multidisc Optim 2021;63:2065–97.
[59] Strand7. Release 3. 2021, www.strand7.com/r3/.
[60] Descamps B, Filomeno Coelho R. The nominal force method for truss geometry and topology optimization incorporating stability considerations. Int J Solids Struct 2014;51(13):2390–9.